Measuring microscale strain fields in articular cartilage during rapid impact reveals thresholds for chondrocyte death and a protective role for the superficial layer

Lena R. Bartell[a], **Lisa A. Fortier**[b], **Lawrence J. Bonassar**[c,d], and **Itai Cohen**[e]

[a]School of Applied and Engineering Physics, Cornell University, Ithaca, NY, USA

[b]Department of Clinical Sciences, Cornell University, Ithaca, NY, USA

[c]Department of Biomedical Engineering, Cornell University, Ithaca, NY, USA

[d]Sibley School of Mechanical and Aerospace Engineering, Cornell University, Ithaca, NY, USA

[e]Department of Physics, Cornell University, Ithaca, NY, USA

Abstract

Articular cartilage is a heterogeneous soft tissue that dissipates and distributes loads in mammalian joints. Though robust, cartilage is susceptible to damage from loading at high rates or magnitudes. Such injurious loads have been implicated in degenerative changes, including chronic osteoarthritis (OA), which remains a leading cause of disability in developed nations. Despite decades of research, mechanisms of OA initiation after trauma remain poorly understood. Indeed, although bulk cartilage mechanics are measurable during impact, current techniques cannot access microscale mechanics at those rapid time scales. We aimed to address this knowledge gap by imaging the microscale mechanics and corresponding acute biological changes of cartilage in response to rapid loading. In this study, we utilized fast-camera and confocal microscopy to achieve roughly 85 μm spatial resolution of the cartilage deformation during a rapid (~3 ms), localized impact and the chondrocyte death following impact. Our results showed that, at these high rates, strain and chondrocyte death were highly correlated (p<0.001) with a threshold of 8% microscale strain norm before any cell death occurred. Additionally, chondrocyte death had developed by two hours after impact, suggesting a time frame for clinical therapeutics. Moreover, when the superficial layer was removed, strain – and subsequently chondrocyte death – penetrated deeper into the samples (p<0.001), suggesting a protective role for the superficial layer of articular cartilage. Combined, these results provide insight regarding the detailed biomechanics that drive early chondrocyte damage after trauma and emphasize the importance of understanding cartilage and its mechanics on the microscale.

Corresponding author: Lena R. Bartell, C7 Clark Hall, Cornell University, Ithaca, NY 14853, Phone: (607) 255-8853, Fax: (607) 255-6428, lrb89@cornell.edu.

Conflict of interest statement

The authors have no financial or personal conflicts of interest to disclose.

Keywords

PTOA; Indentation; Elastography; Arthritis initiation; Injury

1. Introduction

Osteoarthritis involves the degradation of articular cartilage in joints and is a leading cause of disability (Birchfield, 2001; Jackson et al., 2001; Murphy et al., 2008). Clinically, 12% of osteoarthritis is post-traumatic (PTOA), wherein initiation stems from a distinct mechanical insult (Brown et al., 2006) and trauma is known to initiate progressive cartilage degradation (Anderson et al., 2011; Brown et al., 2006; Felson et al., 2000; Fischenich et al., 2015; Goldring and Goldring, 2010; Radin et al., 1972; Vellet et al., 1991). After decades of research, PTOA initiation is poorly understood and a cure remains elusive (Anderson et al., 2011; Goldring and Goldring, 2010; Krasnokutsky et al., 2008; Scott and Athanasiou, 2006).

Understanding PTOA has proven difficult, due in part to the complexities of cartilage material properties and the scope of the disease. For example, cartilage has a distinct superficial layer that is more compliant and dissipates more shear energy than the bulk (Buckley et al., 2013; Schinagl et al., 1996; Silverberg et al., 2014; Wang et al., 2002; Wong et al., 2008). Additionally, a traumatic, pathologic event can deliver forces over a fraction of a second (10^{-3} s) (Aspden et al., 2002, p. 200), while a patient may not present with symptoms for years (10^8 s) (Scott and Athanasiou, 2006). This represents ten orders of magnitude in time that are important to the problem. Currently available animal and explant models can monitor bulk cartilage mechanics on injury time scales (10^{-3} s) and investigate biomechanical effects of trauma over hours to months ($10^1 - 10^6$ s) (Backus et al., 2011; Jeffrey et al., 1995; Newberry et al., 1998; Repo and Finlay, 1977; Scott and Athanasiou, 2006; Waters et al., 2014). Studies have also investigated mechanics at the cellular level (Abusara et al., 2011; Guilak et al., 1995; Upton et al., 2008). Although loading rate affects cellular response (Moo et al., 2013), methods to measure microscale mechanics (e.g. 10–100 μm) at physiologic time scales (e.g. $10^{-1} - 10^0$ s) have only recently been developed (Buckley et al., 2010). This leaves an important, unexplored gap in understanding microscale cartilage changes during and immediately following rapid traumatic injury.

The purpose of this study was to design and implement techniques to investigate the microscale mechanics of articular cartilage during rapid impact and to statistically describe the acute chondrocyte response. In particular, our method correlated microscale tissue strains during rapid impact (85 μm and 1 ms resolutions) with the microscale, time-dependent decrease in cell viability following that impact (85 μm and 10 min resolutions). This correlation enabled identification of microscale thresholds and sensitivities of chondrocytes to microscale deformation. Additionally, we tested for mechanical and biological changes in response with the superficial layer removed. This directly linked the mechanics of rapid cartilage impact to acute biological changes, giving new insight on the mechanisms of PTOA initiation.

2. Methods

A custom method enabled the correlation of chondrocyte death and microscale mechanics: chondral explants were impacted while a fast-camera recorded their rapid deformation; subsequent cell death was captured via confocal microscopy.

2.1. Impact device

The setup consisted of a custom impact device on an inverted confocal microscope (LSM 5 LIVE, Carl Zeiss Inc., Jena, Germany) (Fig. 1) with a 10× objective. The confocal housing interfaced with a high-speed camera (v7.1, Vision Research, Wayne, NJ) and a mercury arc lamp (HBO 100, Carl Zeiss Inc., Germany) to enable epi-fluorescence microscopy at 1,000 frames per second.

The custom impact device (Fig. 1A) includes a spring (2.96 kN/m, McMaster-Carr, Elmhurst, IL) of adjustable compression which, upon triggering, drives a aluminum piston and attached 0.8 mm diameter steel rod (McMaster-Carr, Elmhurst, IL) into the sample (design inspired by Alexander et al. (Alexander et al., 2013)). All impacts were energy-controlled at ~0.12 J (8.9 mm spring compression) to consistently cause cell death without micro-cracking and thus can be considered moderately pathologic (Aspden et al., 2002). Each sample was glued, as described previously (Buckley et al., 2010), to a cantilevered aluminum backplate with the articular surface facing the impact tip. Impacts were observed from below through a glass slide, showing the rod's circular cross section approaching the sample (Fig. 1B). Samples were mounted 2 mm above the glass slide, leaving a fluid layer in between. Using known weights, the backplate was calibrated as a cantilevered spring (152 kN/m). Backplate motion during impact was tracked using intensity-based image correlation in MATLAB (The MathWorks Inc., Natick, MA) and used to measure impact force. Peak force was combined with area of impact indentation to estimate peak bulk stress.

2.2. Sample preparation

Eighteen full-thickness, 6 mm-diameter chondral explants (without bone) were harvested sterilely from the outer rim of the tibial plateau of 6 neonatal calves (sex unknown, assumed random; Gold Medal Packing, Oriskany, NY). Explants were immersed in phenol red-free DMEM with 10% FBS (Invitrogen, Waltham, MA) and 1% antibiotics (100× penicillin-streptomycin, Mediatech, Manassas, VA) and stored at 4°C for up to 48 hours. Using tissue slicer blades (Stadie-Riggs, Thomas Scientific, Swedesboro, NJ), explants were cut in half to create two hemi-cylinders, and trimmed to approximately 2.5 mm deep. Paired hemi-cylinders were used as control and impacted samples. For eight explants, 1 mm was removed from the articular surface, maintaining the 2.5 mm thickness, creating two sample populations: surface-intact and surface-removed.

2.3. High-speed deformation imaging

A fluorescent stain with a photobleached grid was used to visualize tissue motion during impact. All samples were stained in 28 μM 5-DTAF (ex/em 492/516 nm; Invitrogen, Waltham, MA) for 45 minutes followed by a 10-minute PBS rinse to provide general cartilage staining (Buckley et al., 2010; Silverberg et al., 2014). Using a precision wire mesh

(TWP Inc., Berkley, CA) a 120 μm grid was photobleached on the samples. This grid size was chosen to be resolvable over motion blur, ensure adequate cell counting statistics (>50 cells/grid box), and capture tissue mechanical inhomogeneities. Paired control and impact samples were mounted side-by-side to the backplate and surrounded by PBS. Upon impact triggering, cartilage deformation was recorded using the fast camera.

2.4. Cell viability imaging

Chondrocyte death after impact was imaged. 2 uM ethidium homodimer (EthD) (Invitrogen, Waltham, MA) was added to the cavity, staining for 30 minutes before impact. Dead cells were imaged every 10 minutes for 3 hours following impact. Preliminary, 12-hour studies demonstrated that nearly all cell death occurred within 3 hours. To measure total cell density, paired control samples were frozen after experimentation, thawed in PBS, re-stained with EthD and re-imaged (Chen et al., 2001). This produced confocal images of three treatment groups showing: (1) cell death in the impacted sample as a function of time ("impact"), (2) cell death in the control sample as a function of time ("control"), and (3) all cells in the frozen control sample ("frozen"), a measure of the total cell density in that sample. All confocal images were taken in a z-stack spaced at 10 μm to capture dead cells within 40 μm of the cut surface. This spacing was chosen to match the axial resolution of the confocal imaging setup. Images were collapsed in z, normal to the cut surface, before analysis.

2.5. Microscale deformation analysis

To extract microscale cartilage deformation during impact, fast-camera videos were analyzed in MATLAB. The image taken at peak indentation was used as the deformed configuration, with the image just before impact as its reference configuration. For bulk mechanics, displacement of the tissue surface under the impact rod was tracked manually to calculate bulk strain, correcting for backplate displacement. For microscale mechanics, template matching was used to find "bright cross" and "dark square" grid points (blue and yellow circles in Fig. 2A–B). Using nearest-neighbor grid points, the Lagrange strain tensor $E(x, y)$ was calculated with a spatial resolution of roughly 85 μm, where the y-axis is perpendicular to the articular surface (Appendix A). To represent strain as a scalar field, two quantities were computed: the spectral norm of the strain, $||E||$ (strain norm), and the magnitude of the shear component, $|E_{xy}|$ (shear strain).

To characterize the shear strain fields' size and orientation, principal component analysis was performed on the (x, y) points, with a binary weighting based on the shear strain value: 1 for shear strain above 50% of the sample's maximum and 0 otherwise. The first principal component and its orientation relative to undeformed coordinates were extracted, representing the size and orientation of the strain pattern, respectively.

2.6. Cell viability analysis

Confocal images were processed in MATLAB to find (x, y) locations of all dead cells (Appendix B). Through comparison with manual counting, cell counting uncertainty was estimated as 7%. Using Sobel edge detection, the sample surface was identified and fit to a second-order polynomial function of lateral displacement, enabling a correspondence

between spatial coordinates, (x, y), and depth coordinates, (x, d), where d is depth. The same technique was used to compute the depth of each grid point in fast-camera images.

Cell locations were binned to calculate microscale probability of death due to impact as

$P(x, y, t) = \frac{\rho_{\mathrm{impact}}(x,y,t) - \rho_{\mathrm{control}}(x,y,t)}{\rho_{\mathrm{frozen}}(x,y) - \rho_{\mathrm{control}}(x,y,t)}$, where $\rho_i(x, y, t)$ is the area number density of dead cells in each treatment group, i (§2.4), as a function of bin location, (x, y), and time after impact, t. Control densities were subtracted from the numerator and denominator to remove death due to causes other than impact. Roughly 100% cell death was observed at the surface ($\rho_{\mathrm{frozen}} - \rho_{\mathrm{control}} \cong 0$), invalidating analysis there. Thus, data less than 200 μm deep were discarded.

To highlight the time evolution, cells in a 400 μm wide region centered about the impact location were binned at 50 μm in depth (collapsing along the x direction) and used to calculate $P(d, t)$, the probability of death due to impact as a function of depth and time after impact. Trends in $P(d, t)$ were averaged across all samples in each population, where the standard deviation of sample-to-sample variation was roughly 25 percentage points. In MATLAB, a mixed-effects linear regression model was implemented to test for significant differences between data from surface-intact and surface-removed samples. In the model, the response variable was P, while d, t and surface treatment (i.e. intact or removed) were fixed-effect predictor variables, including interaction terms. An independent random effect was added to account for sample to sample variation. Residuals were checked for normality, confirming the model's validity.

2.7. Correlating microscale deformation and viability

Impact deformation and viability following impact were correlated on the microscale. Fast camera grid points in the undeformed configuration (§2.5) were projected onto the confocal image of the same sample at 3 hours after impact. Nearest-neighbor grid points were used as bin boundaries to calculate the microscale probability of cell death due to impact (§2.6). Accordingly, at each grid point (x, d), a correspondence was established between strain norm, $\|E\|$ (§2.5), and probability of death due to impact, P. Fields of $\|E\|$ and P were averaged across sample populations (Appendix C).

A mixed-effects linear regression model tested for the dependence of P on $\|E\|$ and surface treatment. The response variable was P, while d, t, $\|E\|$, and surface treatment were fixed-effect predictor variables, including interactios. In an additional model, $\|E\|$ was used as the response, with d, t, and surface treatment as predictors. In both models, an independent random effect was added to account for sample to sample variation. In all analyses, residuals were checked for normality, confirming the models' validity.

3. Results

3.1. Bulk mechanics

A custom device (Fig. 1) impacted cartilage samples rapidly and consistently (Video 1). Impacts lasted 8 ms, with a time to maximum indentation of 3.7 ± 0.7 ms (mean ± standard deviation). Peak bulk strain and strain rate were $13 \pm 4\%$ and $4 \pm 1 \times 10^3$ %/s. Peak force,

bulk stress, and bulk stress rate were 8 ± 3 N, 2.3 ± 0.9 MPa, and $7 \pm 3 \times 10^2$ MPa/s. Impact time, strain, force, and stress were not significantly different between surface treatment populations, as determined using unpaired, two-tailed t-tests ($p = 0.7$; 0.04; 3; 0.9, respectively). No tissue swelling was observed over the 3-hour experiment.

3.2. Microscale deformation

Microscale strain norm and shear strain during impact were computed from fast-camera images, revealing characteristic maps of each (Fig. 2). Strain norm was highly concentrated near the impact and shear strain fields had two characteristic lobes (Fig. 2C, D). Peak shear strain was lower than peak strain norm. When the superficial layer was removed, strain fields had similar trends but lower values overall (Fig. 3). Shear strain lobes were longer ($p = 0.006$) and oriented more vertically ($p = 0.001$) for surface-removed samples.

3.3. Cell viability

Cell death increased dramatically after impact, showing complex spatial and temporal evolution (Fig. 4). For both sample populations, average probability of death due to impact in the region of interest (orange box) was highest near the surface (Fig. 4C, D). This probability increased with time, though most cell death occurred by 2 hours. Regression modeling confirmed that time, depth, and their interaction were significant predictors of probability of death ($p = 9 \times 10^{-292}$; 4×10^{-30}; 4×10^{-193}, respectively). Cell death in control samples increased over 3 hours, but only 15 percentage points. No dispersal of the EthD stain was observed after freezing.

Comparing surface treatment populations, the peak probability for surface-intact samples was confined to the surface layer while the pattern extended deeper for surface-removed samples ($p = 2 \times 10^{-17}$). Time evolution did not vary significantly between surface treatments ($p = 0.6$).

3.4. Strain and viability correlation

Average strain and probability of death due to impact showed strikingly similar patterns within but not across surface treatment groups (Fig. 5A–D). Both patterns were concentrated near the impact but penetrated deeper with the surface removed ($p = 3 \times 10^{-7}$; 2×10^{-6}, for strain norm and probability of death comparisons). The clear relationship between strain norm and probability of death due to impact ($p = 2 \times 10^{-68}$) was apparent in correlation plots (Fig. 5E, F). This correlation varied slightly, albeit significantly, with depth and surface treatment ($p = 2 \times 10^{-46}$; 1×10^{-13}). For both populations, linear fits revealed a threshold of 8% microscale strain before any cell death occurred and a sensitivity of ~18% strain to produce ~50% probability of cell death at 3 hours.

Correlation was also performed using other Lagrange strain scalars (Appendix D). Some correlations were similarly high ($R^2 = 0.91$; 0.94; 0.95, for the determinant, P2 norm, and deviatoric spectral norm, respectively) while others were lower ($R^2 = 0.11$; 0.05, for shear strain and trace, respectively).

4. Discussion

The goal of this study was to understand the relationship between the microscale mechanical environment in cartilage during rapid loading and subsequent changes in chondrocyte viability. Additionally, we investigated how mechanical heterogeneity mediated chondrocyte response. Thus, a custom method was developed, integrating fast camera and confocal microscopy with spring-loaded impact. This method allowed chondrocyte death to be correlated with rapid tissue deformation on the microscale.

Results showed that, as depicted in Fig. 5, the probability of cell death due to impact was highly correlated with the Lagrange strain norm, enabling the threshold and sensitivity of cells to microscale mechanics to be determined. This correlation was similarly strong for both surface-intact and surface-removed samples, revealing that, for loading at these high rates, strain norm – rather than any depth-dependent cellular sensitivity, for example (Häuselmann et al., 1996) – explains a large majority of the variation in chondrocyte death (93%, for surface-intact samples).

The results further revealed a protective role for the superficial layer. The superficial layer of cartilage is more compliant than the bulk (Buckley et al., 2010; Chahine et al., 2004; Julkunen et al., 2007; Schinagl et al., 1996; Wang et al., 2002; Wong et al., 2008), and thus strain was concentrated in this region, as reflected in Figs. 2 and 3. Since cell death was so highly correlated with strain, it, too, was concentrated in the superficial region of surface-intact samples, as observed previously (Chahine et al., 2007; Chen et al., 2003; Levin et al., 2005; Novakofski et al., 2014; Quinn et al., 2001). However, because impacts were energy controlled, surface-removed samples experienced lower strains at their surface, potentially explaining their lower peak probability of death (Fig. 4C, D). Overall, however, both strain and cell death penetrated significantly deeper after surface removal, reflecting the more homogeneous mechanical properties of the remaining tissue. Thus, by concentrating the strain, the compliant surface layer of healthy cartilage protects the deeper tissue. This novel design principal may be important for the robustness of cartilage and could potentially be applied in other engineering applications, including tissue engineering.

These results may also be useful when interpreting in the context of injury mechanics across many spatial scales. For example, recent studies have incorporated cartilage's mechanical inhomogeneities into models, translating bulk loading into the microscale loading environment (Federico et al., 2005; Li et al., 2003; Wang et al., 2001; Wilson et al., 2005). Given the results of this study, subsequent cell death can be inferred from microscale mechanics at high rates without invasive procedures.

Temporal trends of cell death were also studied. After impact, cell death saturated in about 2 hours (Fig. 4C, D), suggesting a time window following joint trauma in which drugs or therapeutics could be most effective. Notably, as determined by preliminary experiments, EthD could diffuse and stain compromised cells within a few minutes, while an apoptotic response typically develops in hours or days (Del Carlo and Loeser, 2008; D'lima et al., 2001). Thus, the acute chondrocyte death observed here was most likely necrotic, in agreement with Chen et al. (Chen et al., 2001) (Appendix E).

One limitation of this study is the use of immature cartilage, which may be more susceptible to damage (Kurz et al., 2004; Levin et al., 2005). However, immature and mature tissues are mechanically similar (Buckley et al., 2010) and immature tissue provides a consistent framework for studying injury (Li et al., 2013; Rolauffs et al., 2013). Samples also exhibited extensive cell death at the surface, masking surface chondrocytes which may respond differently to loading and potentially altering the sensitivity of nearby, viable cells. This limitation may be overcome by storing samples in culture conditions. Additionally, the impact geometry and the material of the impacting rod did not directly mimic *in vivo* loading. Instead, the unconfined compression and small-diameter impacting rod were used to impose a wide range of strains in the field of view, enabling strain and cell death correlations to be rigorously investigated. Translating loading from the bulk scale to the microscale will depend strongly on the geometry and boundary conditions, potentially affecting cartilage response (Heiner et al., 2013; Jeffrey and Aspden, 2006). However, as a physical property, the microscale strain thresholds would not be expected to change with loading and geometry. Though the source of the strain may not be observed *in vivo*, the general relationship between strain and cell death should hold for a broader variety of loading scenarios at similar rates. It should be noted that, at these length scales, this study cannot measure cellular strains or mechanotransduction mechanisms, but instead measures strain and cell death as continuous distributions on the scale of tissue inhomogeneity (Mow and Guo, 2002).

Previous studies have similarly linked impact mechanics to cartilage damage, both mechanical (e.g. fissuring) and biological (e.g. chondrocyte death) (Chen et al., 1999; Ewers et al., 2001; Huser and Davies, 2006; Jeffrey et al., 1995; Quinn et al., 2001; Repo and Finlay, 1977; Torzilli et al., 1999; Waters et al., 2014). In this study, impacts (0.1 J energy, 2 MPa stress) caused chondrocyte death without fracture, implying that bulk cell death thresholds are below this level while fissuring thresholds are above. This energy is in agreement with cell death thresholds implied or observed previously (Huser and Davies, 2006; Jeffrey et al., 1995), while stress thresholds are typically much higher (Repo and Finlay, 1977, p. 197; Torzilli et al., 1999).

More broadly, previous cartilage impact studies have failed to establish consensus regarding the thresholds and sensitivities of any damage measure to a given loading profile. Existing discrepancies (e.g., (Haut et al., 1995; Natoli et al., 2008; Newberry et al., 1998) may reflect the large variety of impact protocols, geometries and boundary conditions. Moreover, tests in sufficiently different loading scenarios with respect to material behavior (e.g. gel diffusion rate (Morel and Quinn, 2004)) cannot be reliably compared. Bulk measures are also limiting. Because cartilage is spatially inhomogeneous (Stolberg-Stolberg et al., 2013), they may not adequately portray the local cartilage environment. Indeed, even if damage spreads, it is initiated locally – on the cellular scale for biological damage or on the fiber scale for matrix damage.

The method presented here helps clarify how rapid mechanical signals correlate with cell responses. Fast-camera imaging enables the response of a true impact – rather than only the slower, so-called injurious compression – to be investigated on the microscale (Aspden et al., 2002), statistically linking strain and cell viability. Future studies will exploit these

higher spatial and temporal resolutions to better understand damage initiation in cartilage. By varying microscale impact mechanics and geometry (e.g. strain, strain rate, rod size), thresholds and sensitivities of both biological changes and mechanical damage after impact can be determined. Additionally, this setup can address the effectiveness of various drugs and dosage protocols for preventing or reducing acute chondrocyte death. Overall, by studying micrometer- and millisecond-scale responses, this experimental approach provides a powerful tool for clarifying the details of cartilage injury response and PTOA initiation after trauma.

Supplementary Material

Refer to Web version on PubMed Central for supplementary material.

Acknowledgments

References

Abusara Z, Seerattan R, Leumann A, Thompson R, Herzog W. A novel method for determining articular cartilage chondrocyte mechanics in vivo. Journal of Biomechanics. 2011; 44:930–934. [PubMed: 21145552]

Alexander PG, Song Y, Taboas JM, Chen FH, Melvin GM, Manner PA, Tuan RS. Development of a Spring-Loaded Impact Device to Deliver Injurious Mechanical Impacts to the Articular Cartilage Surface. Cartilage. 2013; 4:52–62. [PubMed: 26069650]

Anderson DD, Chubinskaya S, Guilak F, Martin JA, Oegema TR, Olson SA, Buckwalter JA. Post-traumatic osteoarthritis: Improved understanding and opportunities for early intervention. Journal of Orthopaedic Research. 2011; 29:802–809. [PubMed: 21520254]

Aspden RM, Jeffrey JE, Burgin LV. Letter to the Editor. Osteoarthritis and Cartilage. 2002; 10:588–589. [PubMed: 12127840]

Backus JD, Furman BD, Swimmer T, Kent CL, McNulty AL, DeFrate LE, Guilak F, Olson SA. Cartilage viability and catabolism in the intact porcine knee following transarticular impact loading with and without articular fracture. Journal of Orthopaedic Research. 2011; 29:501–510. [PubMed: 21337389]

Birchfield PC. Osteoarthritis overview. Geriatric Nursing. 2001; 22:124–131. [PubMed: 11410762]

Brown TD, Johnston RC, Saltzman CL, Marsh JL, Buckwalter JA. Posttraumatic Osteoarthritis: A First Estimate of Incidence, Prevalence, and Burden of Disease. Journal of Orthopaedic Trauma. 2006; 20:739–744. [PubMed: 17106388]

Buckley MR, Bergou AJ, Fouchard J, Bonassar LJ, Cohen I. High-resolution spatial mapping of shear properties in cartilage. Journal of Biomechanics. 2010; 43:796–800. [PubMed: 19896130]

Buckley MR, Bonassar LJ, Cohen I. Localization of Viscous Behavior and Shear Energy Dissipation in Articular Cartilage Under Dynamic Shear Loading. Journal of Biomechanical Engineering. 2013; 135:031002–031002.

Chahine NO, Ateshian GA, Hung CT. The effect of finite compressive strain on chondrocyte viability in statically loaded bovine articular cartilage. Biomechanics and Modeling in Mechanobiology. 2007; 6:103–111. [PubMed: 16821016]

Chahine NO, Wang CCB, Hung CT, Ateshian GA. Anisotropic strain-dependent material properties of bovine articular cartilage in the transitional range from tension to compression. Journal of Biomechanics. 2004; 37:1251–1261. [PubMed: 15212931]

Chen CT, Bhargava M, Lin PM, Torzilli PA. Time, stress, and location dependent chondrocyte death and collagen damage in cyclically loaded articular cartilage. Journal of Orthopaedic Research. 2003; 21:888–898. [PubMed: 12919878]

Chen CT, Burton-Wurster N, Borden C, Hueffer K, Bloom SE, Lust G. Chondrocyte necrosis and apoptosis in impact damaged articular cartilage. Journal of Orthopaedic Research. 2001; 19:703–711. [PubMed: 11518282]

Chen CT, Burton-Wurster N, Lust G, Bank RA, Tekoppele JM. Compositional and metabolic changes in damaged cartilage are peak-stress, stress-rate, and loading-duration dependent. Journal of Orthopaedic Research. 1999; 17:870–879. [PubMed: 10632454]

Del Carlo M, Loeser RF. Cell death in osteoarthritis. Current Rheumatology Reports. 2008; 10:37–42. [PubMed: 18457610]

D'lima DD, Hashimoto S, Chen PC, Colwell CW, Lotz MK. Human chondrocyte apoptosis in response to mechanical injury. Osteoarthritis and Cartilage. 2001; 9:712–719. [PubMed: 11795990]

Ewers BJ, Dvoracek-Driksna D, Orth MW, Haut RC. The extent of matrix damage and chondrocyte death in mechanically traumatized articular cartilage explants depends on rate of loading. Journal of Orthopaedic Research. 2001; 19:779–784. [PubMed: 11562121]

Federico S, Grillo A, La Rosa G, Giaquinta G, Herzog W. A transversely isotropic, transversely homogeneous microstructural-statistical model of articular cartilage. Journal of Biomechanics. 2005; 38:2008–2018. [PubMed: 16084201]

Felson DT, Lawrence RC, Dieppe PA, Hirsch R, Helmick CG, Jordan JM, Kington RS, Lane NE, Nevitt MC, Zhang Y, Sowers M, McAlindon T, Spector TD, Poole AR, Yanovski SZ, Ateshian G, Sharma L, Buckwalter JA, Brandt KD, Fries JF. Osteoarthritis: New Insights. Part 1: The Disease and Its Risk Factors. Annals of Internal Medicine. 2000; 133:635–646. [PubMed: 11033593]

Fischenich KM, Button KD, Coatney GA, Fajardo RS, Leikert KM, Haut RC, Haut Donahue TL. Chronic changes in the articular cartilage and meniscus following traumatic impact to the lapine knee. Journal of Biomechanics. 2015; 48:246–253. [PubMed: 25523754]

Goldring MB, Goldring SR. Articular cartilage and subchondral bone in the pathogenesis of osteoarthritis. Annals of the New York Academy of Sciences. 2010; 1192:230–237. [PubMed: 20392241]

Guilak F, Ratcliffe A, Mow VC. Chondrocyte deformation and local tissue strain in articular cartilage: A confocal microscopy study. Journal of Orthopaedic Research. 1995; 13:410–421. [PubMed: 7602402]

Häuselmann HJ, Flechtenmacher J, Michal L, Thonar EJMA, Shinmei M, Kuettner KE, Aydelotte MB. The superficial layer of human articular cartilage is more susceptible to interleukin-1–induced damage than the deeper layers. Arthritis & Rheumatism. 1996; 39:478–488. [PubMed: 8607897]

Haut RC, Ide TM, De Camp CE. Mechanical Responses of the Rabbit Patello-Femoral Joint to Blunt Impact. Journal of Biomechanical Engineering. 1995; 117:402–408. [PubMed: 8748521]

Heiner AD, Smith AD, Goetz JE, Goreham-Voss CM, Judd KT, McKinley TO, Martin JA. Cartilage-on-cartilage versus metal-on-cartilage impact characteristics and responses. Journal of Orthopaedic Research. 2013; 31:887–893. [PubMed: 23335281]

Huser CAM, Davies ME. Validation of an in vitro single-impact load model of the initiation of osteoarthritis-like changes in articular cartilage. Journal of Orthopaedic Research. 2006; 24:725–732. [PubMed: 16514652]

Jackson DW, Simon TM, Aberman HM. Symptomatic articular cartilage degeneration: the impact in the new millennium. Clinical Orthopaedics and Related Research. 2001:S14–25. [PubMed: 11603698]

Jeffrey JE, Aspden RM. The Biophysical Effects of a Single Impact Load on Human and Bovine Articular Cartilage. Proceedings of the Institution of Mechanical Engineers, Part H: Journal of Engineering in Medicine. 2006; 220:677–686.

Jeffrey JE, Gregory DW, Aspden RM. Matrix Damage and Chondrocyte Viability Following a Single Impact Load on Articular-Cartilage. Archives of Biochemistry and Biophysics. 1995; 322:87–96. [PubMed: 7574698]

Julkunen P, Kiviranta P, Wilson W, Jurvelin JS, Korhonen RK. Characterization of articular cartilage by combining microscopic analysis with a fibril-reinforced finite-element model. Journal of Biomechanics. 2007; 40:1862–1870. [PubMed: 17052722]

Krasnokutsky S, Attur M, Palmer G, Samuels J, Abramson SB. Current concepts in the pathogenesis of osteoarthritis. Osteoarthritis and Cartilage. 2008; 16:S1–S3. [PubMed: 18723377]

Kurz B, Lemke A, Kehn M, Domm C, Patwari P, Frank EH, Grodzinsky AJ, Schünke M. Influence of tissue maturation and antioxidants on the apoptotic response of articular cartilage after injurious compression. Arthritis & Rheumatism. 2004; 50:123–130. [PubMed: 14730608]

Levin AS, Chen CTC, Torzilli PA. Effect of tissue maturity on cell viability in load-injured articular cartilage explants. Osteoarthritis and Cartilage. 2005; 13:488–496. [PubMed: 15922183]

Li L, Shirazi-Adl A, Buschmann MD. Investigation of mechanical behavior of articular cartilage by fibril reinforced poroelastic models. Biorheology. 2003; 40:227–233. [PubMed: 12454409]

Li Y, Frank EH, Wang Y, Chubinskaya S, Huang HH, Grodzinsky AJ. Moderate dynamic compression inhibits pro-catabolic response of cartilage to mechanical injury, tumor necrosis factor-α and interleukin-6, but accentuates degradation above a strain threshold. Osteoarthritis and Cartilage. 2013; 21:1933–1941. [PubMed: 24007885]

Moo EK, Amrein M, Epstein M, Duvall M, Abu Osman NA, Pingguan-Murphy B, Herzog W. The Properties of Chondrocyte Membrane Reservoirs and Their Role in Impact-Induced Cell Death. Biophysical Journal. 2013; 105:1590–1600. [PubMed: 24094400]

Morel V, Quinn TM. Cartilage injury by ramp compression near the gel diffusion rate. Journal of Orthopaedic Research. 2004; 22:145–151. [PubMed: 14656673]

Mow VC, Guo XE. Mechano-electrochemical properties of articular cartilage: Their inhomogeneities and anisotropies. Annual Review of Biomedical Engineering. 2002; 4:175–209.

Murphy L, Schwartz TA, Helmick CG, Renner JB, Tudor G, Koch G, Dragomir A, Kalsbeek WD, Luta G, Jordan JM. Lifetime risk of symptomatic knee osteoarthritis. Arthritis Care & Research. 2008; 59:1207–1213. [PubMed: 18759314]

Natoli RM, Scott CC, Athanasiou KA. Temporal Effects of Impact on Articular Cartilage Cell Death, Gene Expression, Matrix Biochemistry, and Biomechanics. Annals of Biomedical Engineering. 2008; 36:780–792. [PubMed: 18299988]

Newberry WN, Garcia JJ, Mackenzie CD, Decamp CE, Haut RC. Analysis of Acute Mechanical Insult in an Animal Model of Post-traumatic Osteoarthrosis. Journal of Biomechanical Engineering. 1998; 120:704–709. [PubMed: 10412452]

Novakofski KD, Williams RM, Fortier LA, Mohammed HO, Zipfel WR, Bonassar LJ. Identification of cartilage injury using quantitative multiphoton microscopy. Osteoarthritis and Cartilage. 2014; 22:355–362. [PubMed: 24185113]

Quinn TM, Allen RG, Schalet BJ, Perumbuli P, Hunziker EB. Matrix and cell injury due to sub-impact loading of adult bovine articular cartilage explants: effects of strain rate and peak stress. Journal of Orthopaedic Research. 2001; 19:242–249. [PubMed: 11347697]

Radin E, Paul I, Rose R. Role of mechanical factors in pathogenesis of primary osteoarthritis. The Lancet. 1972; 299:519–522. Originally published as Volume 1, Issue 7749.

Repo RU, Finlay JB. Survival of articular cartilage after controlled impact. The Journal of Bone & Joint Surgery. 1977; 59:1068–1076. [PubMed: 591538]

Rolauffs B, Kurz B, Felka T, Rothdiener M, Uynuk-Ool T, Aurich M, Frank E, Bahrs C, Badke A, Stöckle U, Aicher WK, Grodzinsky AJ. Stress-vs-time signals allow the prediction of structurally catastrophic events during fracturing of immature cartilage and predetermine the biomechanical, biochemical, and structural impairment. Journal of Structural Biology. 2013; 183:501–511. [PubMed: 23810923]

Schinagl DRM, Ting MK, Price JH, Sah RL. Video microscopy to quantitate the inhomogeneous equilibrium strain within articular cartilage during confined compression. Annals of Biomedical Engineering. 1996; 24:500–512. [PubMed: 8841725]

Scott CC, Athanasiou KA. Mechanical Impact and Articular Cartilage. Critical Reviews™ in Biomedical Engineering. 2006; 34:347–378.

Silverberg JL, Barrett AR, Das M, Petersen PB, Bonassar LJ, Cohen I. Structure-Function Relations and Rigidity Percolation in the Shear Properties of Articular Cartilage. Biophysical Journal. 2014; 107:1721–1730. [PubMed: 25296326]

Stolberg-Stolberg JA, Furman BD, William Garrigues N, Lee J, Pisetsky DS, Stearns NA, DeFrate LE, Guilak F, Olson SA. Effects of cartilage impact with and without fracture on chondrocyte viability and the release of inflammatory markers. Journal of Orthopaedic Research. 2013; 31:1283–1292. [PubMed: 23620164]

Torzilli PA, Grigiene R, Borrelli JJ, Helfet DL. Effect of Impact Load on Articular Cartilage: Cell Metabolism and Viability, and Matrix Water Content. Journal of Biomechanical Engineering. 1999; 121:433–441. [PubMed: 10529909]

Upton ML, Gilchrist CL, Guilak F, Setton LA. Transfer of Macroscale Tissue Strain to Microscale Cell Regions in the Deformed Meniscus. Biophysical Journal. 2008; 95:2116–2124. [PubMed: 18487290]

Vellet AD, Marks PH, Fowler PJ, Munro TG. Occult posttraumatic osteochondral lesions of the knee: prevalence, classification, and short-term sequelae evaluated with MR imaging. Radiology. 1991; 178:271–276. [PubMed: 1984319]

Wang CCB, Deng JM, Ateshian GA, Hung CT. An Automated Approach for Direct Measurement of Two-Dimensional Strain Distributions Within Articular Cartilage Under Unconfined Compression. Journal of Biomechanical Engineering. 2002; 124:557–567. [PubMed: 12405599]

Wang CCB, Hung CT, Mow VC. An analysis of the effects of depth-dependent aggregate modulus on articular cartilage stress-relaxation behavior in compression. Journal of Biomechanics. 2001; 34:75–84. [PubMed: 11425083]

Waters NP, Stoker AM, Carson WL, Pfeiffer FM, Cook JL. Biomarkers affected by impact velocity and maximum strain of cartilage during injury. Journal of Biomechanics. 2014; 47:3185–3195. [PubMed: 25005436]

Wilson W, van Donkelaar CC, van Rietbergen R, Huiskes R. The role of computational models in the search for the mechanical behavior and damage mechanisms of articular cartilage. Medical Engineering & Physics, Advances in the finite element modelling of soft tissue deformation. 2005; 27:810–826.

Wong BL, Bae WC, Chun J, Gratz KR, Lotz M, Sah Robert L. Biomechanics of cartilage articulation: Effects of lubrication and degeneration on shear deformation. Arthritis & Rheumatism. 2008; 58:2065–2074. [PubMed: 18576324]
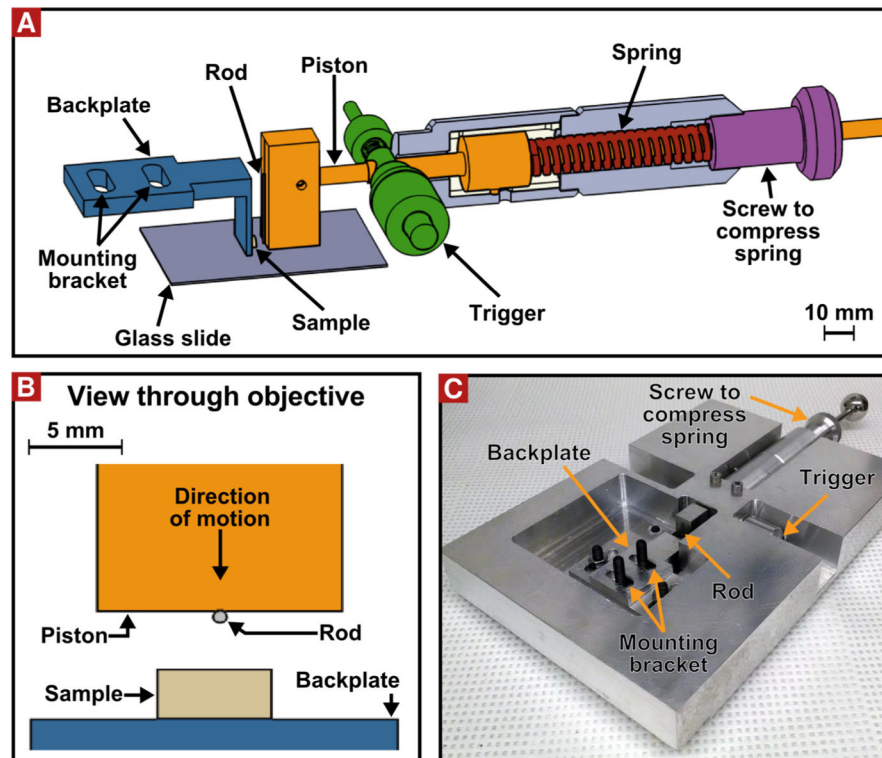
Figure 1.
A technique for rapid impact microscopy was developed. A custom impact device (A, B) included a compressed spring which was released by a trigger to drive the piston and attached rod into the sample. The sample, which was mounted on the backplate, was immersed in PBS to maintain tissue hydration during testing. The cantilevered backplate was mounted to the stable body of the impact device via a mounting bracket. A glass slide allowed the sample to be viewed from below. The impact device was designed to mount on an inverted confocal microscope such that the objective looks up through the glass slide, as depicted (B). The microscope also interfaced with a mercury arc lamp and high-speed camera (not shown) to allow epifluorescence imaging at 1,000 frames per second. (C) A photograph of the impact device.
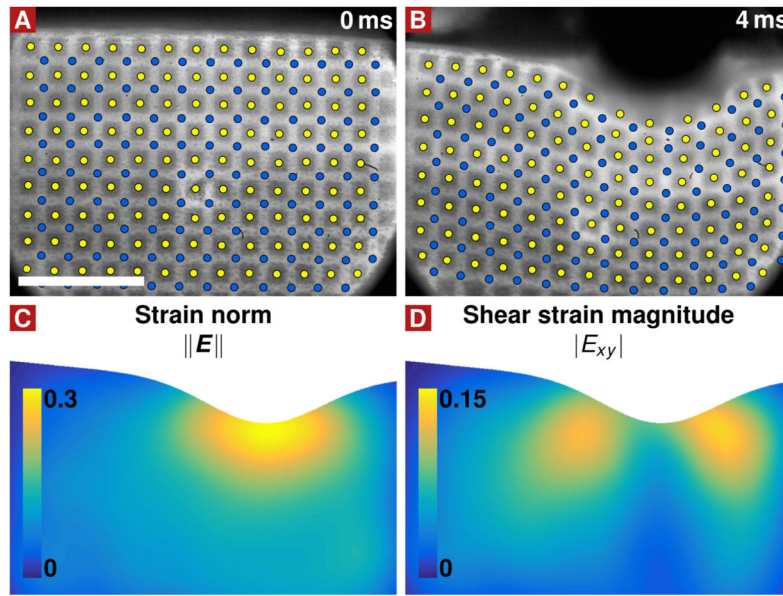
Figure 2.
Representative fast-camera images of rapid cartilage impact and associated microscale strain fields. Fast-camera images taken before impact (A) and at peak indentation (B) were processed to extract grid-point locations (blue and yellow circles). This grid was divided into nearest-neighbor triangles, which were tracked between frames and used to extract the microscale Lagrange strain tensors. Note that dark triangles in the bottom left and right of (A, B) are the edge of the circular field of view, while the flat edge at the top is the surface of the sample. Representative maps of the spectral norm of the Lagrange strain (C) and the magnitude of the Lagrange shear component (D), both shown with respect to deformed spatial coordinates, demonstrate characteristic patterns of strain localization. The scale bar is 500 μm and applies to all plots.
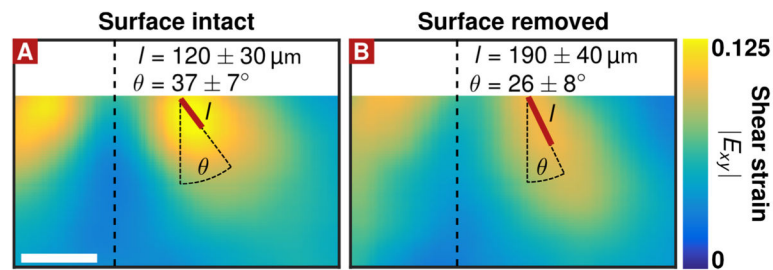
Surface intact

$l = 120 \pm 30\,\mu m$
$\theta = 37 \pm 7°$

Surface removed

$l = 190 \pm 40\,\mu m$
$\theta = 26 \pm 8°$

Shear strain $|E_{xy}|$

0.125

0

Figure 3.
Average microscale shear strain patterns show variations with surface treatment. As compared to surface-intact samples (A), the lobes in surface-removed samples (B) became significantly more elongated ($p = 0.006$) and more vertically aligned ($p = 0.001$), based on principal component analysis. The dashed line indicates the axis of impact in each plot. The scale bar is 250 μm and the color and scale bars apply to both plots.
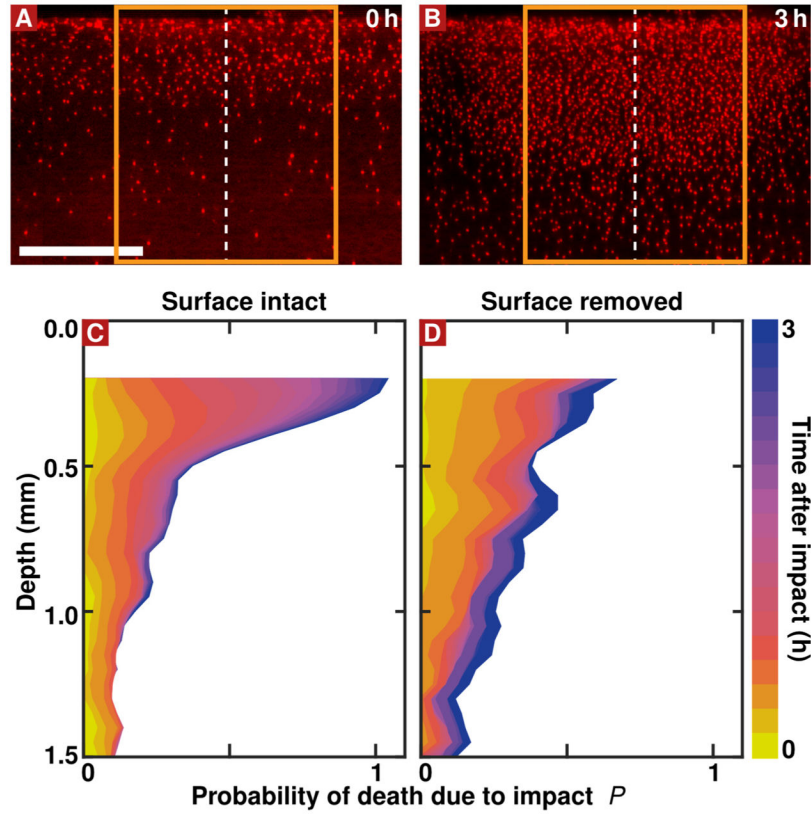
Figure 4.
Spatial and temporal evolution of chondrocyte death after impact. A representative confocal image sequence shows dead chondrocytes in an impacted, surface-intact sample immediately following impact (A) and 3 hours after impact (B). Both images show the same location and the dashed line indicates the axis of impact. Plots (C, D) reflect the time- and depth-dependent increase in probability of cell death after impact, calculated from the region of interest (orange box) and averaged over all samples for surface-intact (C) and surface-removed (D) sample populations. With the surface intact, the peak is more confined to the superficial layer ($p = 2 \times 10^{-17}$). Depths less than 200 μm were excluded because this region exhibited nearly 100% death, invalidating analysis at these points. The scale bar is 250 μm.
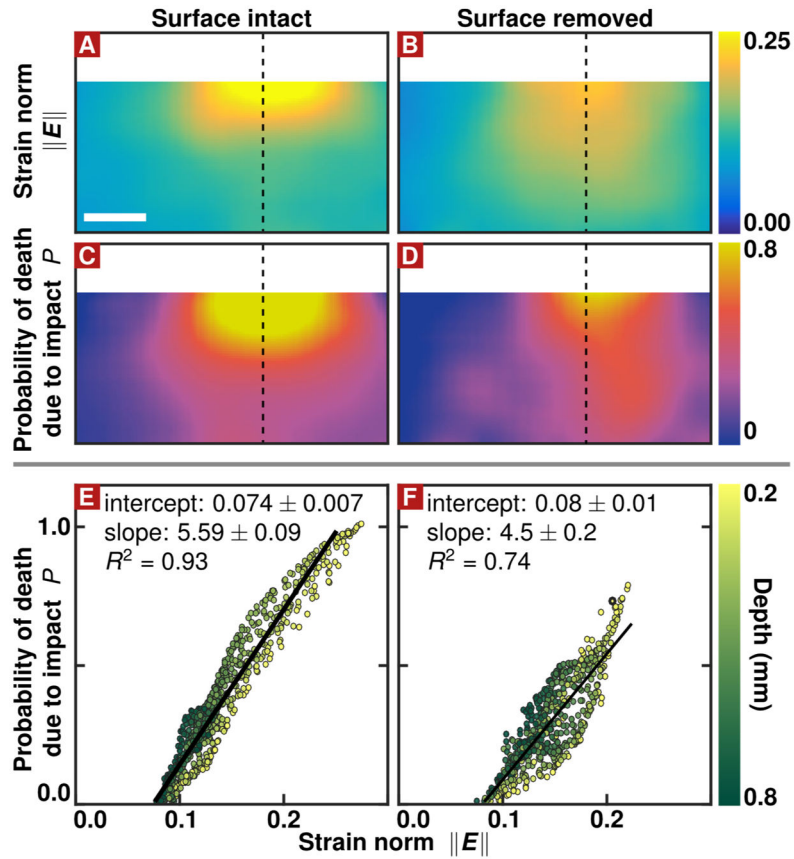
Figure 5.
Microscale patterns of strain norm (A, B) and probability of death (C, D) averaged over all samples in each surface-treatment population show strikingly similar patterns within a given population. Average patterns are shown for both surface-intact (A, C) and surface-removed (B, D) populations and all data are plotted with respect to undeformed spatial coordinates. Both strain and chondrocyte death penetrated deeper into the samples when the superficial layer of cartilage was removed ($p = 3 \times 10^{-7}$; 2×10^{-6}). The dashed line indicates the axis of impact in each plot. Additionally, the probability of cell death after impact was strongly correlated with the microscale strain norm for all samples with the surface intact (E) or removed (F) ($p = 2 \times 10^{-68}$). In these plots, each data point represents one point from the tracked fast-camera grid of one sample, and takes on values corresponding to the microscale strain and probability of death due to impact in the corresponding region of that sample. Points are color-coded based on their depth from the sample surface. Linear fits are shown for each population and the text indicates the strain-axis intercept (threshold), the slope (sensitivity), and the coefficient of determination (R^2) of the fit. As before, data within 200 μm of the surface were omitted. The scale bar is 250 μm and applies to A–D.